World Electric Vehicle Journal

MDPI

Article

Multi-Objective Lightweight Optimization and Decision for CTB Battery Box Under Multi-Condition Performance

Junming Huang [1,*], Shangyuan Ling [1], Shichao Zhang [2], Pinpin Qin [1], Juncheng Lu [2] and Kaiyu Meng [1]

[1] School of Mechanical Engineering, Guangxi University, Nanning 530004, China; 2311391068@st.gxu.edu.cn (S.L.); qpinpin@gxu.edu.cn (P.Q.); 2311391091@st.gxu.edu.cn (K.M.)
[2] Guangxi Huge Stone New Energy Technology Co., Ltd., Nanning 530009, China; shichao.zhang@hugestone-js.com (S.Z.); rujacking@163.com (J.L.)
* Correspondence: jmhuang@gxu.edu.cn

Abstract

To address the conflicts among objectives and the decision-making challenges in the multi-condition adaptive design of battery boxes for new energy vehicles, this study proposes a multi-objective collaborative optimization method based on an improved relaxation factor, aiming to achieve a comprehensive enhancement in both structural lightweighting and mechanical performance. A finite element model of the CTB high-strength steel roll-formed battery box was established and validated through modal testing. According to the Chinese National Standard GB 38031-2025, the mechanical responses of the battery box under random vibration, extreme operating conditions, and impact loads were analyzed to identify performance weaknesses. Sensitivity analysis was conducted to screen the design variables, and an improved relaxation factor strategy based on weight distribution difference information was introduced to construct a multi-objective collaborative optimization model. Furthermore, the entropy-weighted TOPSIS method was employed to enable intelligent decision-making on the Pareto solution set. The results demonstrate that the proposed method outperforms conventional approaches in both convergence speed and solution distribution uniformity. After optimization, the mass of the battery box was reduced by 12.38%, while multiple mechanical performance indicators were simultaneously improved, providing valuable theoretical and engineering guidance for the structural design of power battery systems.

Keywords: CTB; battery box; multi-objective optimization; relaxation factor

Check for updates

Academic Editor: Michael Fowler

Received: 23 November 2025
Revised: 26 December 2025
Accepted: 30 December 2025
Published: 6 January 2026

Copyright: © 2026 by the authors. Published by MDPI on behalf of the World Electric Vehicle Association. Licensee MDPI, Basel, Switzerland. This article is an open access article distributed under the terms and conditions of the Creative Commons Attribution (CC BY) license.

1. Introduction

In recent years, with the steady increase in the penetration rate of new energy vehicles (NEVs), they have gradually replaced traditional internal combustion engine vehicles. As a result, NEVs are becoming the main direction for the future development of the automotive industry. As a critical assembly widely used in NEVs, the power battery system plays a key role in ensuring vehicle safety, performance, and endurance. However, conventional battery module designs face limitations in accommodating a larger number of cells within restricted installation spaces [1]. Therefore, achieving structural lightweighting through cell-to-body (CTB) integration technology has become an important approach to improving driving range and reducing energy consumption in electric vehicles. Among various structural solutions, the CTB battery box fabricated using high-strength steel

roll-forming technology has attracted growing attention from original equipment manufacturers due to its advantages in cost efficiency, lightweight potential, and platform adaptability [2]. To further strengthen battery safety standards, the Chinese National Standard GB 38031-2025 [3], titled Safety Requirements for Traction Battery Systems of Electric Vehicles, will come into effect in July 2026. Under this new regulation, designers of power battery systems face a significant challenge in achieving lightweight CTB battery boxes while satisfying the multi-condition strength requirements specified in the standard. At the same time, identifying optimization directions and strategies for existing products to comply with the updated safety requirements has become a key issue in power battery system design.

The CTB battery box has become a research hotspot due to its high level of integration and strong performance potential. Existing studies have mainly focused on improving its performance from three aspects, namely structural innovation, material application, and optimization methodology. In the field of structural design, Lian et al. [1] investigated the frontal crash safety of CTB structures and achieved compliance with the intrusion requirements of the front bulkhead while maintaining controllable deformation of the battery pack, providing a valuable reference for the body design of pure electric vehicles. Zhao et al. [4] proposed a novel CTB battery pack featuring an inward concave triangular microstructure, and the optimized structure exhibited significantly enhanced mechanical performance, reducing the maximum intrusion displacement during collision by 3.2%. Qiao et al. [5] conducted finite element analysis (FEA) combined with experimental validation to perform local structural optimization at the lug connection area of the battery box, which effectively reduced the maximum stress in this region. Likewise, Li et al. [6] utilized finite element analysis and structural optimization techniques to reduce the vibration fatigue risk of a fast-swapping battery box for electric vehicles while achieving overall structural lightweighting.

In terms of materials and hybrid structures, Duan et al. [7] applied a multi-stage optimization approach to conduct lightweight design of the upper cover assembly of a CTB battery pack, focusing on variable rib beams (VRB) and hybrid structures. Their results showed that the VRB/OW-GFRP hybrid structure achieved a mass reduction of 18.7%. Zeng et al. [8] reported that silicone foam can effectively address the sealing challenges caused by through-type steps and grooves in CTB structures by using coating fillers, thereby meeting the IPX7 protection standard. Zhang et al. [9] performed a multi-objective optimization design of an electric vehicle battery enclosure and identified carbon nanotube (CNT) composites as the optimal material, which reduced stress levels and increased the resonance frequency. The effectiveness of the optimized design was further verified through simulation and analysis.

At the methodological level, extensive research has been carried out by scholars worldwide to enhance optimization techniques for battery structure design. Yue Xiong et al. [10] applied orthogonal experimental design, the response surface method (RSM), and a multi-island genetic algorithm (MIGA) to optimize an electric vehicle battery pack system, achieving an 11.73% weight reduction while improving crashworthiness. Gnanasekar Naresh et al. [11] utilized finite element analysis (FEA) combined with multi-objective optimization techniques to optimize the structural parameters of an electric vehicle battery box, effectively enhancing both structural efficiency and resonance performance. Ma et al. [12] optimized a race car battery box structure through sensitivity analysis and the GRNN–NSGA-II method, achieving a 15.1% reduction in mass while maintaining torsional stiffness and natural frequency, with computational efficiency improved by 323.8%. Arslan and Karamangil [13] developed a glass-fiber-reinforced polymer (GFRP) hybrid side panel for battery boxes that combined honeycomb and auxetic structures, leading

to a 23.9% mass reduction and a 3% improvement in crash performance through multi-objective optimization. Yay et al. [14] applied a multi-objective optimization approach to an aluminum-foam-filled battery box and, based on the NSGA-II algorithm, improved side-pole impact performance by increasing specific energy absorption by 50.7% and reducing peak force by 11.6%. Wang Ningzhen et al. [15] employed a response surface model coupled with a multi-objective genetic algorithm (MOGA) to optimize an electric vehicle battery box, significantly enhancing vibration performance while achieving lightweighting. Su et al. [16] proposed a general multidisciplinary design optimization (MDO) framework, referred to as DMPS-MDOF, based on an adaptive disciplinary surrogate model, which improved optimization efficiency. Cui et al. [17] utilized an evolutionary algorithm to perform multidisciplinary design optimization of an electric vehicle battery pack, achieving enhanced structural performance and overall lightweight design. Hao Qi et al. [18] adopted a multidisciplinary optimization approach based on a radial basis function (RBF) surrogate model to design an electric vehicle door, achieving both lightweighting and improved mechanical performance.

A review of the above studies indicates that although considerable progress has been achieved in specific scenarios, a common scientific challenge remains. Existing optimization approaches for CTB battery boxes face significant difficulties in addressing the complex coupling and conflicts among multiple working conditions (e.g., compression, impact, and vibration) and multiple objectives (e.g., lightweighting, crashworthiness, and stiffness). Traditional response surface method (RSM)–based multi-objective optimization approaches exhibit low efficiency when dealing with high-dimensional design variables and objectives. Although collaborative optimization (CO) frameworks can improve computational efficiency, their system-level coordination mechanisms are often static or empirically defined, limiting their ability to dynamically adapt to complex interdisciplinary conflicts under multi-condition constraints. Consequently, the optimization process tends to suffer from unstable convergence and unevenly distributed Pareto solution sets, which undermines the reliability of final engineering decisions. To address this issue, the present study focuses on the key challenge of multi-condition performance CO of CTB battery boxes by developing a method capable of effectively coordinating objective conflicts, improving optimization efficiency, and enhancing the quality of the solution set. On the basis of CO, a relaxation factor is introduced to quantify the inconsistency between subsystem and system-level design variables. To overcome the convergence difficulties and local optimality problems caused by empirically defined relaxation factors, an improved CO algorithm is proposed, which enables a more scientific and adaptive characterization of the trade-offs among subdisciplines, thereby enhancing the robustness and engineering applicability of the optimization process. Furthermore, the entropy-weighted TOPSIS method is employed to evaluate and select from the Pareto solution set, ensuring that the final design scheme is determined in a scientific and objective manner. The main contributions of this study are summarized as follows.

(1) Based on the technical requirements of the Chinese National Standard GB 38031-2025, a simulation study is conducted on a specific type of CTB battery box to identify structural design deficiencies. The results provide valuable references for subsequent multi-condition structural optimization and future studies under the new standard.
(2) The traditional dynamic relaxation factor is improved, and a multi-condition CO of the CTB battery box is carried out using the CO method. This approach achieves lightweighting while simultaneously enhancing the static–dynamic performance and crashworthiness of the battery box.
(3) By integrating the improved CO approach with the entropy-weighted TOPSIS decision-making method, a systematic “optimization–decision” framework is estab-

lished, providing a methodological reference for performance trade-off analysis and design scheme selection of battery enclosures under multiple constraint conditions.

2. Static and Dynamic Analysis of the CTB Battery Box

2.1. Establishment of the Finite Element Model and Modal Test Validation of the Battery Box

The CTB high-strength steel roll-formed battery box consists of the upper cover plate, bottom guard plate, front and rear frames, left and right side beams, mounting beams, cross and longitudinal beams, and lifting lugs. The upper cover and the bottom guard plate are connected to the lower box assembly using bolts. In contrast, the side beams are welded to the mounting beams, while the frames are welded to the lifting lugs. In addition, the cross and longitudinal beams are joined through welding. The total mass of the battery box is 81.896 kg. In the finite element modeling, bolted joints are equivalently represented by beam elements to efficiently capture the force and moment transfer behavior of bolts, thereby simplifying the model and improving computational efficiency. Welded joints are simulated using dedicated welding elements, which avoid artificial stiffness and redundant contact calculations while enabling accurate definition of weld material properties, thus ensuring solution accuracy with acceptable computational cost. Considering the structural and mechanical characteristics of the traction battery enclosure components, a differentiated meshing strategy is adopted. Thin-walled components (e.g., the enclosure assembly, upper cover, and bottom guard plate) are discretized using shell elements, whereas battery cell modules are meshed with hexahedral solid elements. Element sizes are determined by load-bearing importance and geometric complexity: 5 mm for primary load-carrying beams, 10 mm for secondary structural components, and 15 mm for battery cells. Since the research focuses primarily on the battery box itself, the battery module model is geometrically simplified by omitting detailed features such as wires and terminals [19]. The simplified finite element model of the battery box is shown in Figure 1.

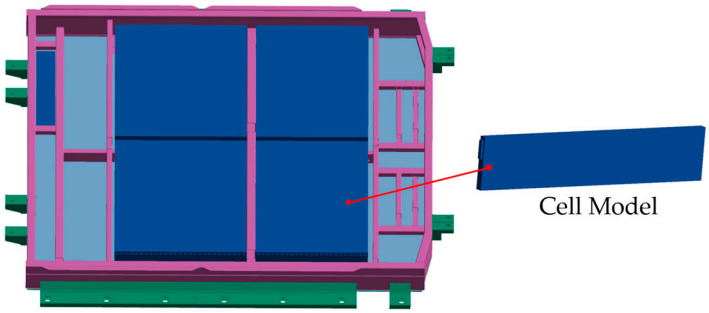


Figure 1. Finite element model of the CTB battery box.

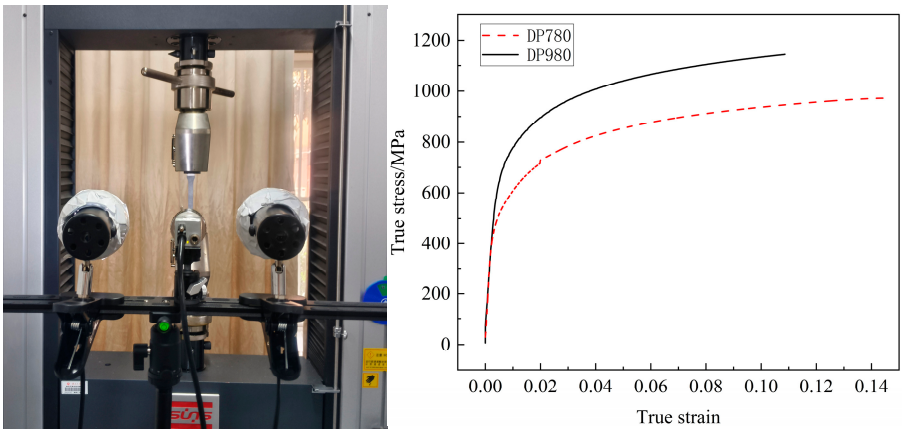
In the CTB high-strength steel roll-formed battery box, the left and right side beams and the mounting beams are made of DP980 high-strength steel, while the front and rear frames are made of DP780 high-strength steel. The bottom guard plate primarily consists of DP980 high-strength steel sheets and glass-fiber-reinforced polypropylene (PP-GF) panels. The upper cover mainly uses resin-based composite (PCM) panels and polypropylene (PP) panels. The cross and longitudinal beams are made of Q235 steel, and the lifting lugs are made of 10B21 steel. The battery cells are modeled as a homogenized equivalent model, as the focus of this study is on the mechanical response of the battery enclosure rather than the micromechanical behavior of the internal cell structure. The blade batteries used in the battery enclosure have a density of approximately 2700 kg/m^3, which is comparable to that of aluminum, and their key mechanical properties, such as Young's modulus and Poisson's ratio, are likewise comparable to those of aluminum. Moreover, due to the relatively large distance between the cells and the side beams in the lateral direction, the expansion force

generated during battery charge and discharge has a negligible effect on the box structure. Similarly, in the longitudinal direction, buffer structures are present between the cells and the cross beams, further reducing the influence of expansion forces. Additionally, the weld joints of the high-strength steel enclosure exhibit strength levels close to those of the base metal. Therefore, during the modeling process, the battery cells are directly assigned aluminum material properties [20]. The physical properties of the main materials used in the battery cell components are listed in Table 1.

Table 1. Main material parameters of the battery box.

Material	Density (kg·m^{-3})	Poisson's Ratio	Elastic Modulus (MPa)	Yield Strength (MPa)
DP 980	7850	0.28	215,000	550
DP 780	7850	0.3	206,000	420
Q235	7850	0.3	210,000	235
10B21	7800	0.29	210,000	249
Al	2700	0.35	70,000	100
PCM	1950	0.4	26,500	—
PP	920	0.44	1370	30
PP-GF	1610	0.25	15,900	60

To accurately simulate the nonlinear deformation and failure behavior of the primary load-bearing structures of the battery enclosure under crash or overload conditions, the main components are modeled using material plasticity models based on actual experimental data. The plastic deformation of the battery enclosure is primarily concentrated in the side and bottom regions. The main components are made of DP780 and DP980 high-strength steels, whose complete engineering stress–strain curves were obtained from uniaxial tensile tests and converted into true stress–strain curves for direct input into the finite element simulations. The experimental setup and the resulting true stress–strain curves are shown in Figure 2.



(**a**) (**b**)

Figure 2. Uniaxial tensile test setup and data: (**a**) The uniaxial tensile test setup; (**b**) True Stress–Strain Curve.

Modal analysis of the battery system serves as an effective criterion for evaluating the rationality of the product design at the initial stage. Among various modes, constrained modes can more accurately reflect the dynamic characteristics of connected structural components [21]. Based on the connection relationship between the power battery system and the vehicle body, the six degrees of freedom at the mounting beam holes and lifting lug holes are constrained, and a modal simulation is performed. When the first-order

natural frequency of the battery structure is higher than 30 Hz, resonance can be effectively avoided [22]. The simulation shows that the first-order modal frequency of the battery box is 32.512 Hz, exceeding the road excitation frequency range and indicating that resonance will not occur. The first six natural frequencies and their corresponding mode shapes of the battery box are listed in Table 2 and shown in Figure 3.

Table 2. Natural frequencies and corresponding mode shape characteristics.

Order	Natural Frequency (Hz)	Mode Shape Description
1	32.512	First-order bending vibration in the Z direction at the center of the upper cover
2	51.232	Second-order bending vibration in the Z direction at both ends of the upper cover
3	64.147	Third-order bending vibration in the Z direction at the center of the upper cover
4	65.733	Fourth-order bending vibration in the Z direction at the front of the upper cover
5	89.458	Fifth-order bending vibration in the Z direction at the front and rear of the upper cover
6	94.545	Sixth-order bending vibration in the Z direction at both sides of the upper cover

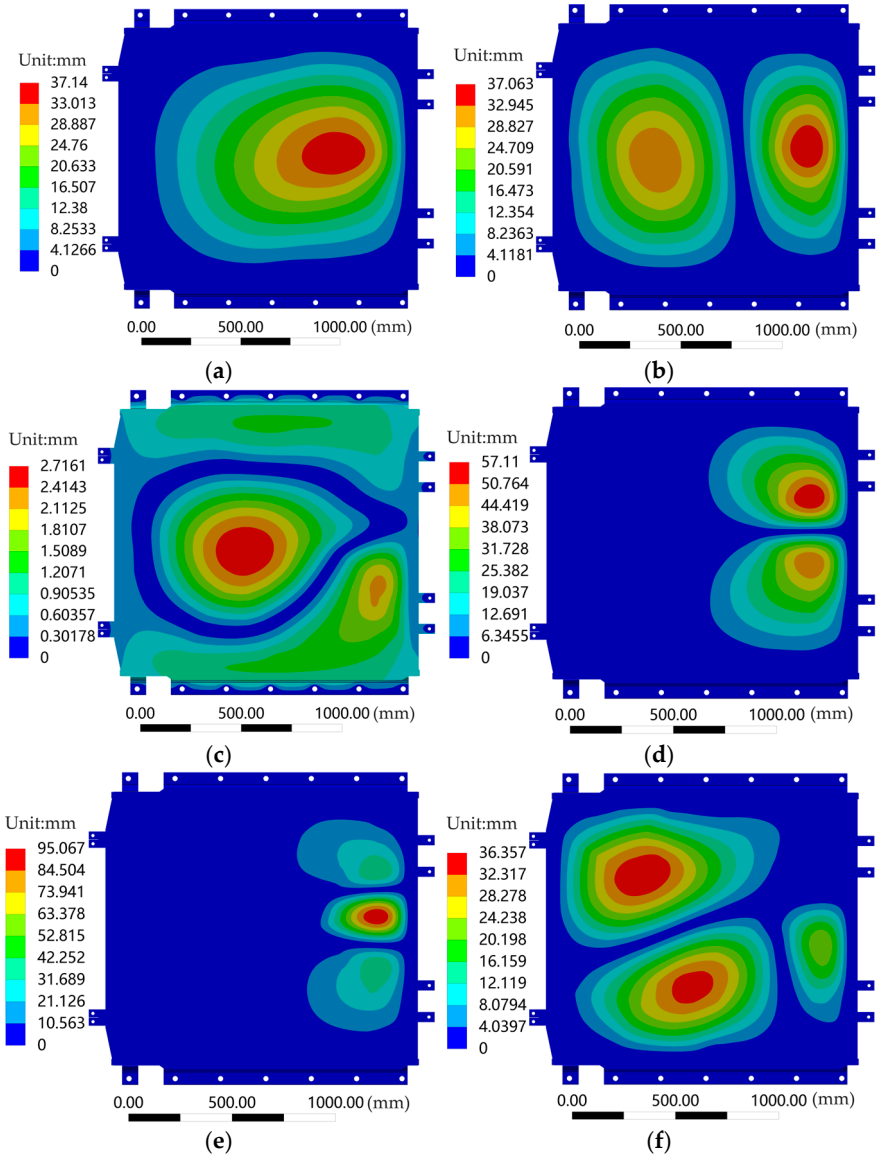


Figure 3. First six mode shapes: (**a**) 1st mode shape; (**b**) 2nd mode shape; (**c**) 3rd mode shape; (**d**) 4th mode shape; (**e**) 5th mode shape; (**f**) 6th mode shape.

Given that the reliability of numerical predictions must be validated through uncertainty analysis, this study investigates the first-order natural modal frequency of the battery box. The primary sources of uncertainty arise from material properties, boundary conditions, and geometric tolerances. A Monte Carlo simulation with 2000 iterations was performed to obtain the probabilistic distribution of the first-order natural frequency under variations in the input parameters, as presented in Figure 4.

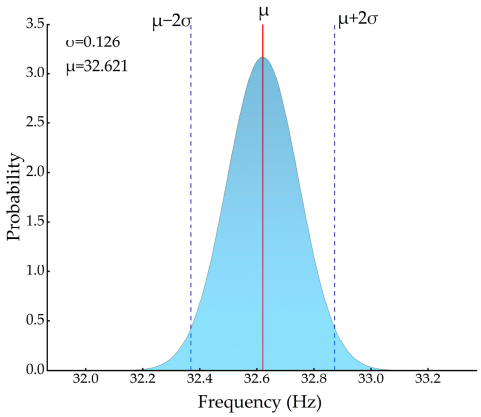


Figure 4. Frequency uncertainty analysis.

The results show that the first-order natural frequency follows an approximately normal distribution, with a mean (μ) of 32.621 Hz and a standard deviation (σ) of 0.126 Hz. The initial simulation value of 32.512 Hz lies within the 2σ interval [32.37 Hz, 32.87 Hz], corresponding to a confidence level of approximately 95.45%. These results confirm the stability of the simulation model under reasonable variations in the input parameters, while the lower bound of the confidence interval remains above the safety threshold of 30 Hz, ensuring the safety of the design.

To further verify the simulation-based modal analysis results, a modal test was conducted on the CTB high-strength steel roll-formed battery box. The test system consisted mainly of an excitation device, accelerometers, and a data acquisition system, as summarized in Table 3. A total of 36 data acquisition points were arranged for the test, and the corresponding experimental setup and the battery box are shown in Figures 5 and 6, respectively.

Table 3. List of testing equipment.

Instrument Name	Instrument Model	Relevant Parameters
Data Acquisition System	DH5902N	Frequency Range: DC–100 kHz
Force Hammer	LC02	Sensitivity: 0.834757 mV/N
Accelerometer	1A202E	Sensitivity: 100.2 mV/(m/s^2)
Test Analysis Software	DHDAS	—

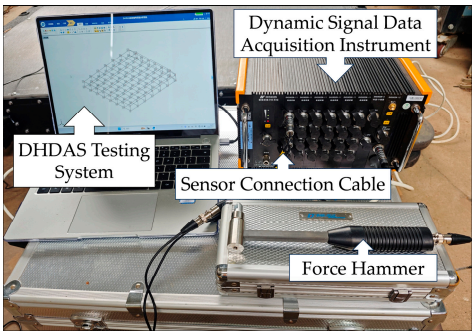


Figure 5. Testing equipment.

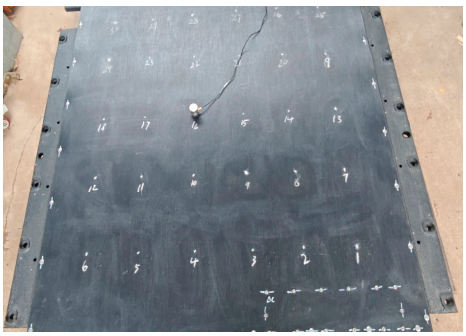


Figure 6. Physical battery box.

The modal parameters of the battery box were extracted through frequency response function (FRF) analysis using the DHDAS testing system. First, the geometric model of the modal test was imported into the software, and the corresponding measurement points were arranged as shown in Figure 7, with point numbers and parameters for the impact hammer and accelerometers properly configured. The single-point excitation and multi-point response method was adopted. Each measurement point on the battery box was impacted five times using an impact hammer, and the vibration signals were acquired through linear averaging. The stabilization diagram of the battery box was obtained using the PolyLSCF (Polynomial Least Squares Complex Frequency) modal parameter identification method, as illustrated in Figure 8.

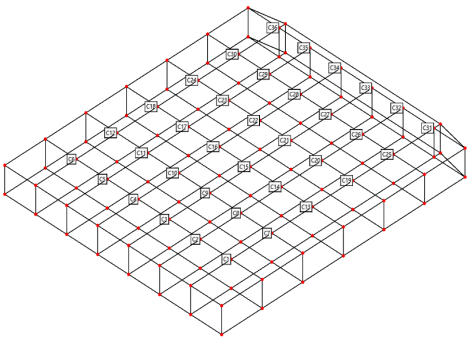


Figure 7. Geometric model for modal testing.

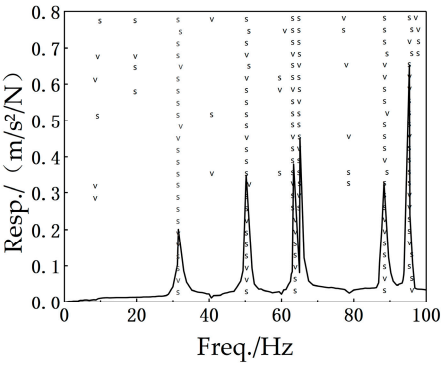


Figure 8. Steady-state diagram of the modal test.

The modal parameters of the battery box were extracted from the stabilization diagram. A comparison between the simulated and experimental natural frequencies is presented in Table 4. The results show that the maximum error between the first six natural frequencies obtained from simulation and experiment is 3.11%, while the minimum error is 0.88%. The close agreement between the simulation and experimental results verifies the accuracy and validity of the established finite element model of the battery box.

Table 4. Comparison of natural frequencies.

Order	Natural Frequency/Hz		Relative Error (%)
	Simulation	Experiment	
1	32.512	31.5	3.11%
2	51.232	50.25	1.92%
3	64.147	63.367	1.22%
4	65.733	65.125	0.92%
5	89.458	88.354	1.23%
6	94.545	95.375	0.88%

2.2. Random Vibration Analysis

In engineering practice, the three-zone method of dynamic stress distribution is commonly used to analyze the stress response under random vibration conditions [23]. In this method, the Von Mises stress is assumed to follow a normal distribution and is divided into three stress zones: $-\sigma_F \sim \sigma_F$, $-2\sigma_F \sim 2\sigma_F$, and $-3\sigma_F \sim 3\sigma_F$. The probabilities of vibration occurring within these three stress zones are 68.3%, 95.4%, and 99.73%, respectively, and the standard deviation of the stress distribution, denoted as σ_F, is obtained from the simulation results as the von Mises stress. According to the vibration test requirements specified in the Chinese National Standard GB 38031-2025, "Electric vehicles traction battery safety requirements", a random vibration simulation analysis was conducted on the battery box. Steady-state random excitations were applied in the X, Y, and Z directions, and the corresponding power spectral density (PSD) values are presented in Table 5, where RMS represents the root mean square value of acceleration.

Table 5. Loading excitation PSD values.

Frequency/Hz	PSD/($g^2 \cdot Hz^{-1}$)		
	X Axis	Y Axis	Z Axis
5	0.006	0.002	0.015
10	—	0.005	—
15	—	—	0.015
20	—	0.005	—
30	0.006	—	—
65	—	—	0.001
100	—	—	0.001
200	0.00003	0.00015	0.0001
RMS	0.50g	0.45g	0.64g

Under random excitations applied in the X, Y, and Z directions, the maximum dynamic stress values of the battery box were statistically analyzed based on a normal distribution, as shown in Table 6. The dynamic stress is relatively high within the range of $-3\sigma_F \sim 3\sigma_F$, and the corresponding cloud diagram of the von Mises stress is shown in Figure 9.

Table 6. Maximum dynamic stress of the battery box in each direction.

Direction	$1\sigma_F$/MPa	$2\sigma_F$/MPa	$3\sigma_F$/MPa
X-axis	5.2292	10.458	15.688
Y-axis	6.4006	12.801	19.202
Z-axis	190.72	381.43	572.15

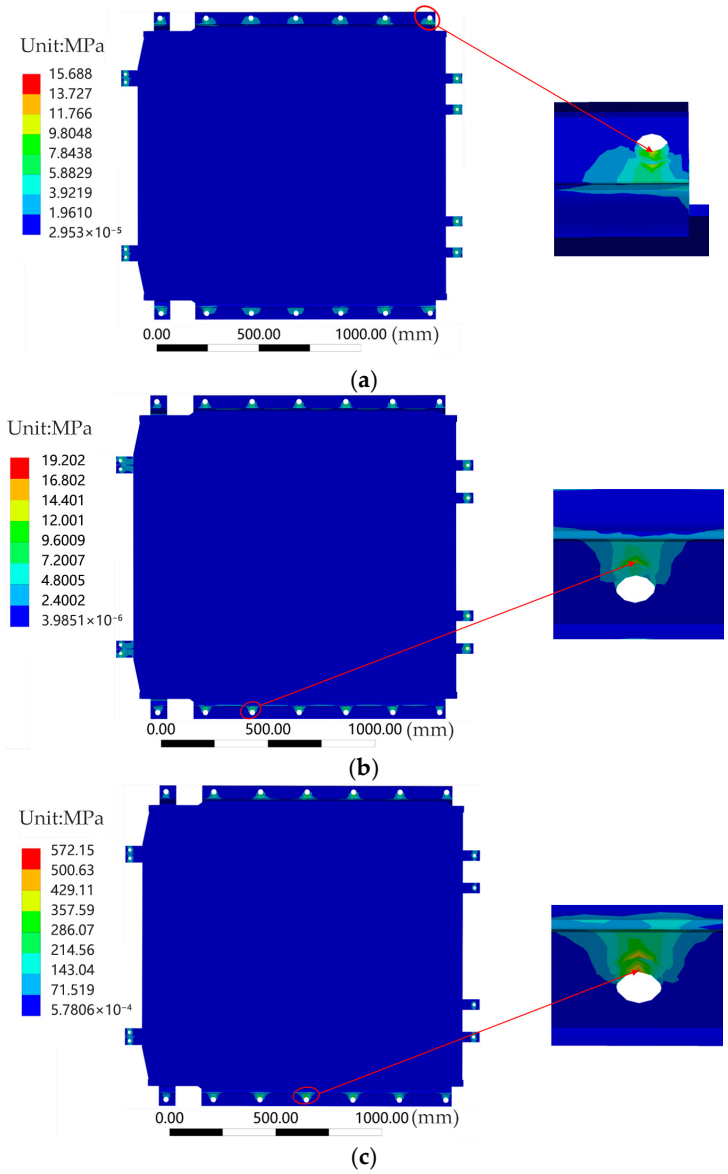


Figure 9. Cloud diagram of von Mises stress under random vibration: (**a**) X direction; (**b**) Y direction; (**c**) Z direction.

The simulation results indicate that under random vibrations in all three directions, the maximum stress is concentrated at the mounting beam joints. In the Z direction, within the range of $-3\sigma_F \sim 3\sigma_F$, the maximum stress reaches 572.15 MPa, which slightly exceeds the material's yield strength of 550 MPa. Therefore, the mounting beam requires structural reinforcement.

2.3. Static Analysis Under Extreme Operating Conditions

In the static analysis of typical extreme operating conditions for vehicles, the maximum stress in the battery box must remain below the material's yield strength. Based on practical conditions and relevant literature [24], three representative extreme operating conditions were selected for the load-bearing analysis. The applied loading scenarios for each condition are summarized in Table 7.

Table 7. Inertial load conditions under typical extreme scenarios.

Typical Extreme Condition	Inertial Load Magnitude/g		
	X (Longitudinal)	Y (Lateral)	Z (Normal)
Vertical Bump	0 g	0 g	3 g
Bump + Emergency Braking	1 g	0 g	2 g
Bump + Sharp Turning	0 g	0.8 g	2 g

The stress cloud diagrams of the battery box under various typical extreme operating conditions are shown in Figure 10. The results indicate that the vertical bump road condition generates the maximum stress of 327.52 MPa, which is significantly lower than the material's yield strength of 550 MPa. This corresponds to a safety factor of 1.68, demonstrating a sufficient structural safety margin.

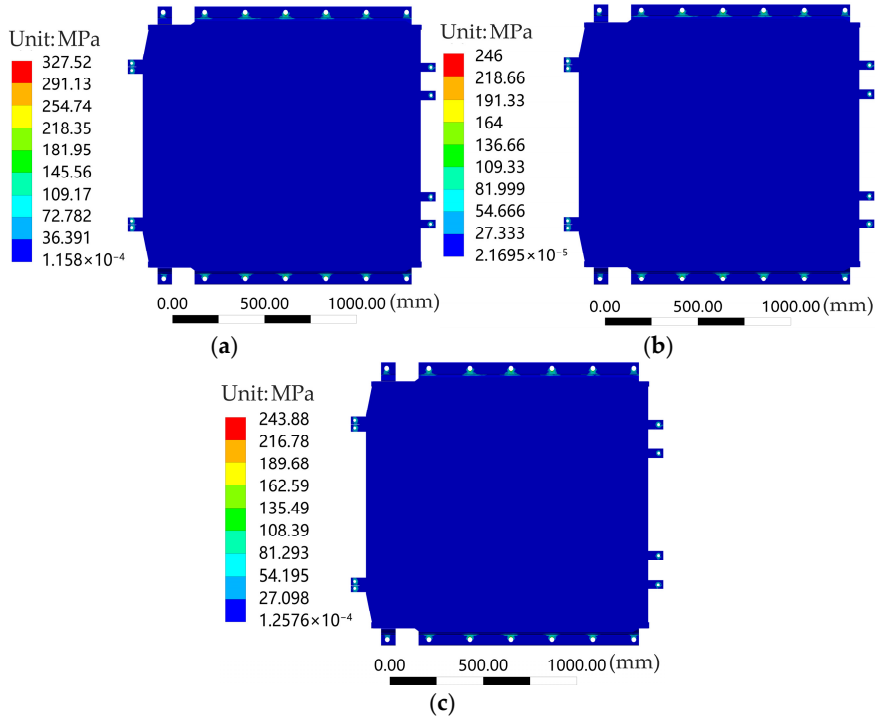


Figure 10. Stress distributions under extreme conditions: (**a**) Vertical bump; (**b**) Bumpy braking; (**c**) Bumpy turn.

3. Crashworthiness Analysis of the Battery Box Side and Bottom

3.1. Side Pole Compression Analysis of the Battery Box

For the side pole compression analysis of the battery box, the compression test was conducted in accordance with the requirements specified in GB 38031-2025 "Electric vehicles traction battery safety requirements". A semicylindrical indenter with a radius of 75 mm and a length greater than the height of the battery box, but not exceeding 1 m, was applied along the X and Y directions. The compression was terminated when the applied load reached 100 kN or when the deformation reached 30% of the overall dimension. The finite element models for X and Y direction compression are shown in Figure 11.

Through simulation analysis, the maximum deformation intrusion of the side beam under X direction compression was 116.01 mm, while the safety clearance in the X direction was 120 mm. For the Y direction compression condition, the maximum displacement of the battery box was 94.315 mm, and the maximum deformation intrusion of the side beam was 19.718 mm, compared with a safety clearance of 40 mm. Therefore, the battery

box meets safety requirements under both X and Y direction compression conditions. The displacement cloud diagram and the variation curves of compression force versus maximum side beam deformation under X and Y direction pole compression are shown in Figures 12 and 13, respectively.

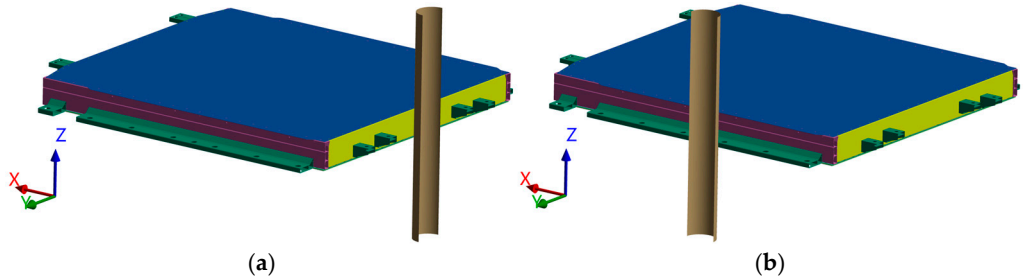


Figure 11. Side pole compression model of the battery box: (**a**) X direction; (**b**) Y direction.

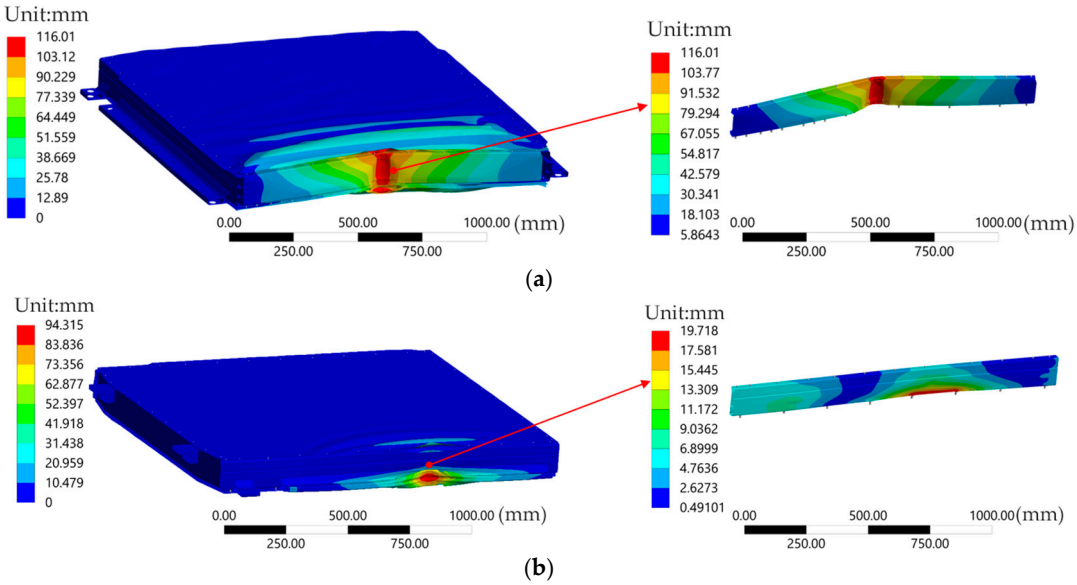


Figure 12. Displacement cloud diagram of the battery box under side pole compression condition: (**a**) X direction; (**b**) Y direction.

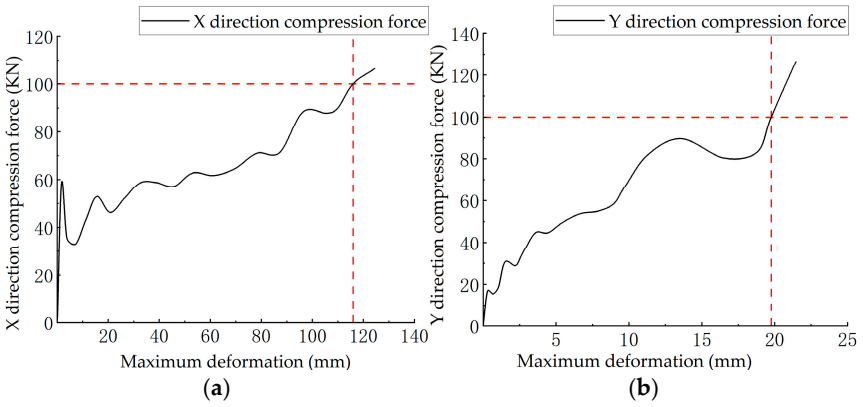


Figure 13. The variation curves of compression force versus maximum side beam deformation: (**a**) X direction; (**b**) Y direction.

3.2. Bottom Impact Analysis of the Battery Box

During vehicle operation, the underside of the body may be subjected to impacts from hard objects. Therefore, the design of the battery box must ensure that its weak

regions possess sufficient resistance to external collisions and impacts. To address the lack of bottom impact requirements in GB 38031-2020, the updated standard GB 38031-2025 introduces supplementary provisions. In this study, a hemispherical impactor with a diameter of 30 mm and a mass of 10 kg was used to strike the three critical protection points on the bottom of the battery box with an impact energy of 150 J. The maximum Z direction displacement of the impactor must remain below the defined safety clearance. The finite element model of the bottom impact condition is shown in Figure 14.

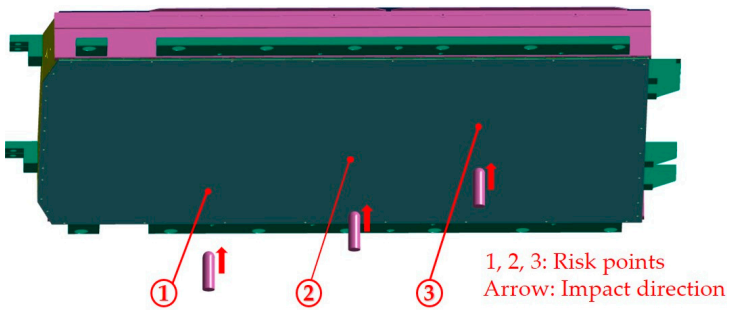


Figure 14. Finite element model of battery box bottom impact.

According to the specified requirements, a finite element simulation was conducted, and the displacement contours at the three bottom protection risk points of the battery box are shown in Figure 15. The results indicate that the central risk point (Point 2) exhibited the largest deformation, with a maximum displacement of 9.1445 mm. The bottom safety clearance of the CTB high-strength steel roll-formed battery box was 10.8 mm, ensuring that the bottom impact did not cause any damage to the battery cells. Therefore, the initial design stiffness of the battery box meets the requirements of the new national standard.

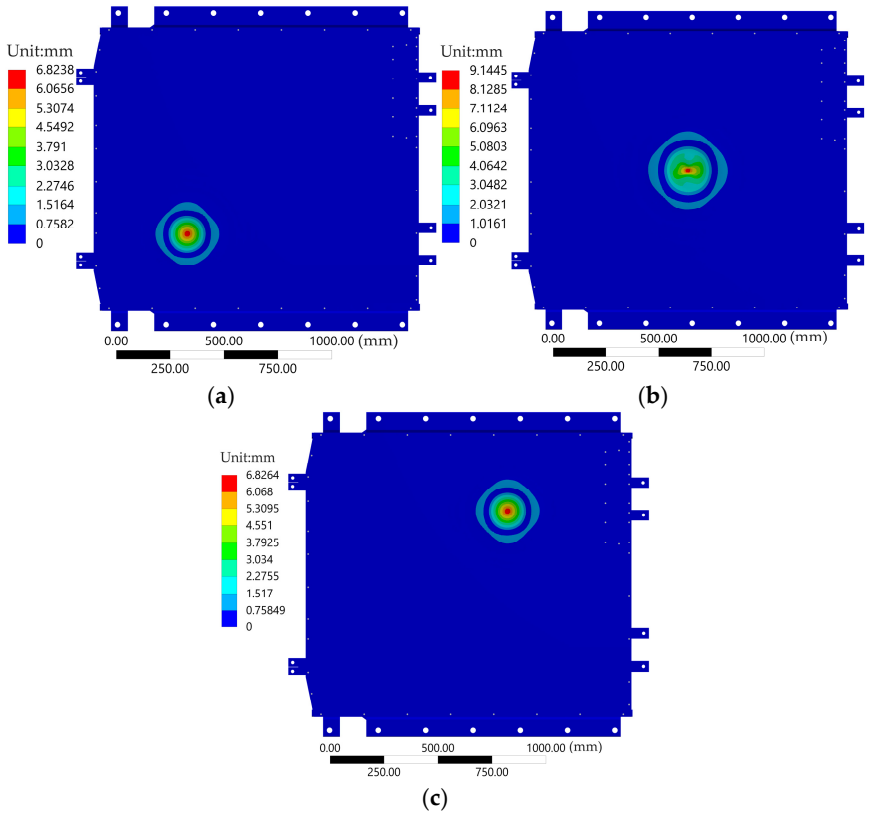


Figure 15. Displacement cloud diagram of the battery box under bottom impact condition: (**a**) Risk point 1; (**b**) Risk point 2; (**c**) Risk point 3.

4. Crashworthiness Analysis of the Battery Box Under Side and Bottom Impact

4.1. Parameter Design and Disciplinary Decomposition

In the multi-condition optimization process of the CTB battery box, traditional multi-objective optimization methods often suffer from local optima and low computational efficiency, while the coupling relationships among design variables lead to interference between optimization objectives. Therefore, a specialized optimization approach is required. Collaborative Optimization [25] is a primary design method within Multidisciplinary Design Optimization [26], which adopts a hierarchical architecture. At the disciplinary level, sub-optimizations are performed within the design domains defined by shared variables, coupling variables, and local variables, minimizing the deviation between local solutions and system-level objectives while satisfying local constraints. At the system level, a dynamic constraint strategy is employed to coordinate inter-domain coupling consistency and drive the search toward a global optimum. Through bidirectional data interaction between the two levels, iterative convergence is achieved, ultimately yielding a system-level optimal solution with consistent cross-disciplinary variables. The principle of this method is illustrated in Figure 16.

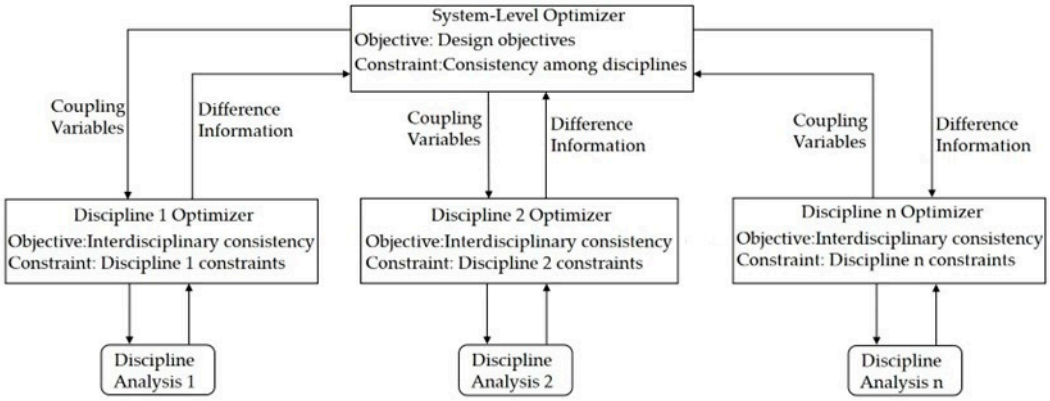


Figure 16. Schematic diagram of the CO design principle.

Based on the concept of CO, the side pole compression condition was defined as Sub-discipline 1, the bottom impact condition as Sub-discipline 2, and the typical extreme operating condition as Sub-discipline 3. According to the simulation analyses of each operating condition and the influence of individual components on the overall performance of the battery box, the thickness parameters of 13 structural components (T_1, T_2, . . ., T_{13}) were selected as optimization design variables, as shown in Figure 17. The initial values and optimization ranges of these variables are listed in Table 8.

Table 8. Ranges and initial values of design variables.

No.	Variable Description	Lower Limit/mm	Upper Limit/mm	Initial Value/mm
T_1	Hanger Beam	0.8	1.6	1.2
T_2	Side Beam	0.8	1.6	1.2
T_3	Side Frame	0.8	1.6	1.2
T_4	Hanger Cross Beam	0.8	1.6	1.2
T_5	Cross Beam 1	0.7	1.3	1.0
T_6	Cross Beam 1	0.7	1.3	1.0
T_7	Upper Cover Plate 1	0.6	1.0	0.8

Table 8. *Cont.*

No.	Variable Description	Lower Limit/mm	Upper Limit/mm	Initial Value/mm
T_8	Upper Cover Plate 2	0.5	0.9	0.7
T_9	Bottom Guard Plate 1	0.7	1.3	1.0
T_{10}	Bottom Guard Plate 2	0.5	1.0	0.8
T_{11}	Bottom Guard Plate 3	0.5	1.0	0.8
T_{12}	Bottom Reinforcement Plate	1.0	2.3	1.5
T_{13}	Cooling Protection Plate	1.6	3.0	2.3

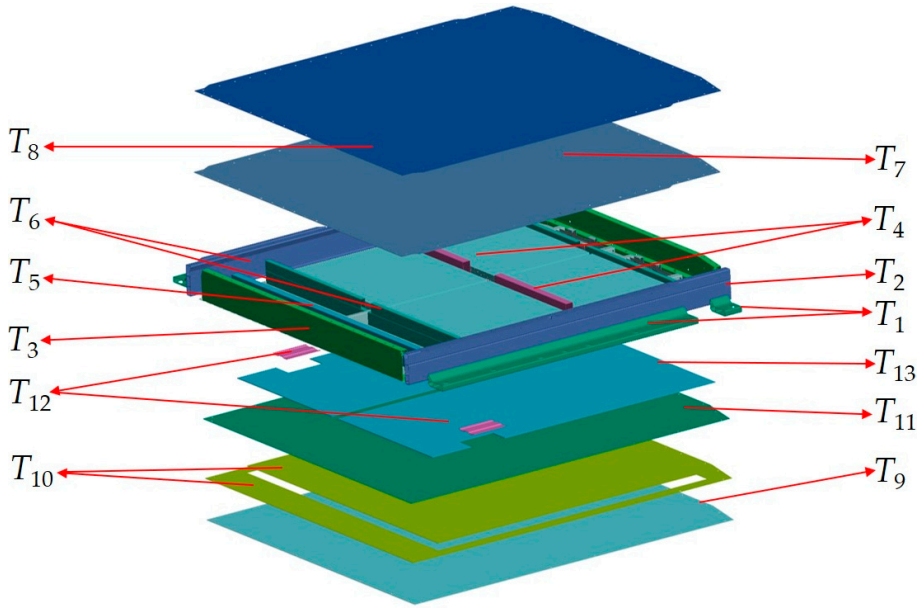


Figure 17. Design variables for battery box optimization.

The sensitivity analysis of the battery box primarily evaluates the influence of variations in component dimensions on stress and deformation. The local sensitivities of the 13 design variables with respect to the three sub-disciplines are illustrated in Figure 18, where the positive and negative signs indicate positive and negative correlations, respectively.

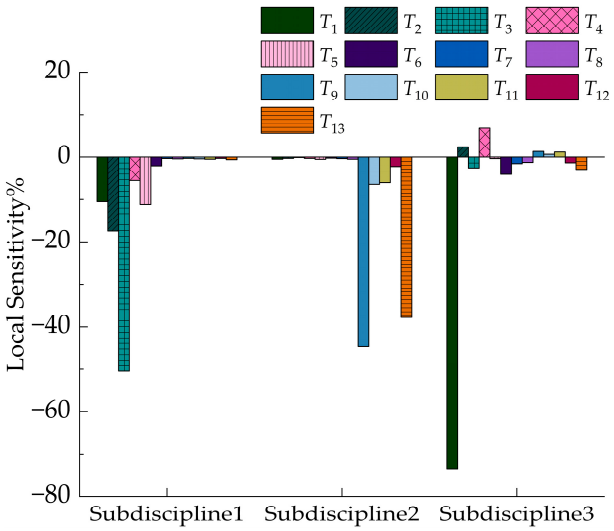


Figure 18. Local sensitivity.

According to the influence of each variable on the sub-disciplines obtained from the sensitivity analysis, the design variables for the three sub-disciplines are defined as shown in Table 9.

Table 9. Local design variables of each subdiscipline.

Subdiscipline 1	Subdiscipline 2	Subdiscipline 3
T_1, T_2, T_3, T_4, T_5, T_6	T_9, T_{10}, T_{11}, T_{12}, T_{13}	T_1, T_2, T_3, T_4, T_6, T_7, T_8, T_9, T_{11}, T_{12}, T_{13}

Based on the design requirements of each sub-discipline and the results of the sensitivity analysis, the coupling relationships among the design variables were determined, as illustrated in Figure 19. Specifically, F_{11} and F_{12} represent the maximum deformations of the side beams under X and Y direction compression, respectively; F_{21} denotes the maximum deformation under the bottom impact condition; and F_{31}, F_{32}, and F_{33} correspond to the maximum stresses under the three extreme operating conditions. The existence of shared cross-disciplinary design variables among the three sub-disciplines indicates strong coupling interactions, further confirming the necessity of CO.

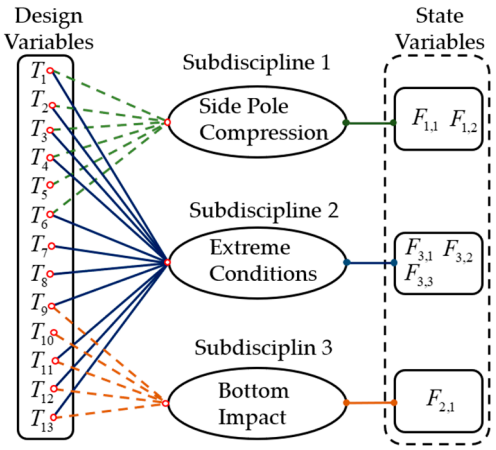


Figure 19. Coupling relationships of design variables.

4.2. Construction and Error Verification of the Surrogate Model

The surrogate models constructed under different working conditions often exhibit varying levels of fitting accuracy. To enhance the overall reliability of the surrogate models, it is advisable to select the most accurate approximation model for each specific working condition. In addition, during the sampling stage, it is generally recommended that the number of samples be no less than $10n$ (where n is the number of design variables). This empirical guideline is widely adopted in engineering practice and helps ensure the predictive stability and generalization capability of the models within complex design spaces. Therefore, for the construction of system-level approximation models, polynomial response surface methodology (RSM) was employed to establish surrogate models for mass, modal, and random vibration conditions, with 150 sample points collected for each case. For Sub-discipline 1, corresponding to the X and Y direction pole compression conditions, 100 sample points were collected, and surrogate models were developed using RSM and the orthogonal polynomial method (OPM), respectively. For Sub-discipline 2, representing the bottom impact condition, 80 sample points were collected, and an RSM-based surrogate model was established. For Sub-discipline 3, corresponding to the typical extreme operating condition, 130 sample points were collected, and a surrogate model was constructed using the radial basis function (RBF) neural network method. The response

surface approximation models of several representative operating conditions are illustrated in Figure 20.

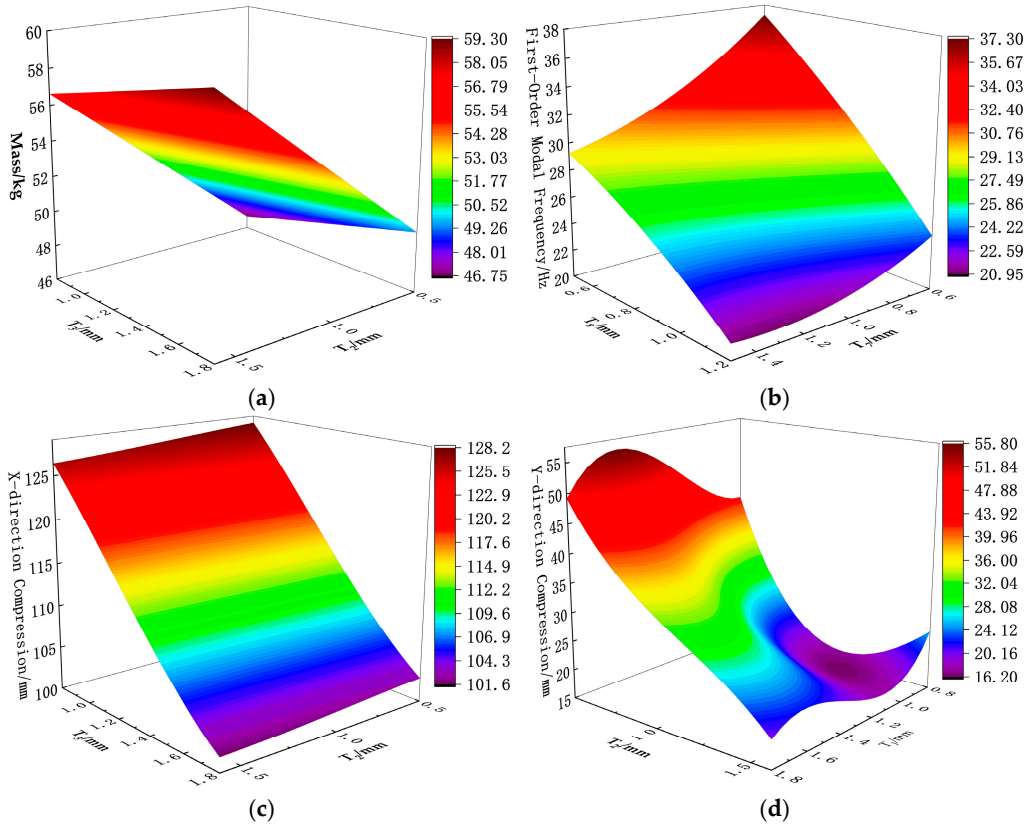


Figure 20. Response surface approximation model: (**a**) Mass and T_2/T_3; (**b**) Modal frequency and T_7/T_8; (**c**) X direction compression and T_2/T_3; (**d**) X direction compression and T_1/T_2.

The fitting analysis between the predicted values of the surrogate models and the finite element simulation results was performed, and the fitting curves are shown in Figure 21. The accuracy indicators of the surrogate models under different operating conditions are summarized in Table 10.

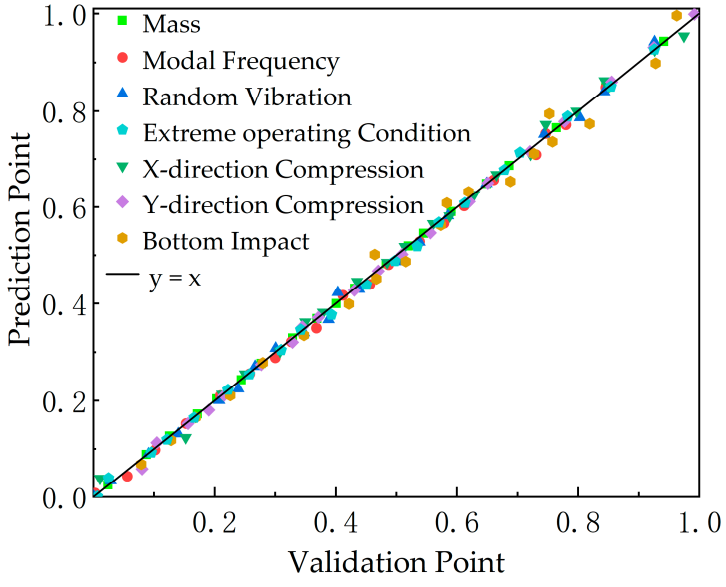


Figure 21. Fitting curve.

Table 10. Accuracy evaluation metrics of the surrogate model.

Design Response	Accuracy Evaluation Metrics			
	e_{avg}	e_{max}	e_{RMS}	R^2
Mass	0.000001	0.000002	0.000001	1
Modal Frequency	0.04408	0.14053	0.05571	0.96012
Random Vibration	0.06301	0.14801	0.07096	0.96272
X-direction Compression	0.01819	0.04560	0.0222	0.99300
Y-direction Compression	0.04160	0.11186	0.05055	0.96598
Bottom Impact	0.03091	0.23561	0.05832	0.96035
Extreme Condition	0.02291	0.08958	0.02845	0.98724

The residual plots effectively evaluate the fitting accuracy of the surrogate models in key regions, such as high-stress zones and primary areas of interest, thereby verifying the reliability of their predictions. The residual plots of several representative surrogate models are presented in Figure 22.

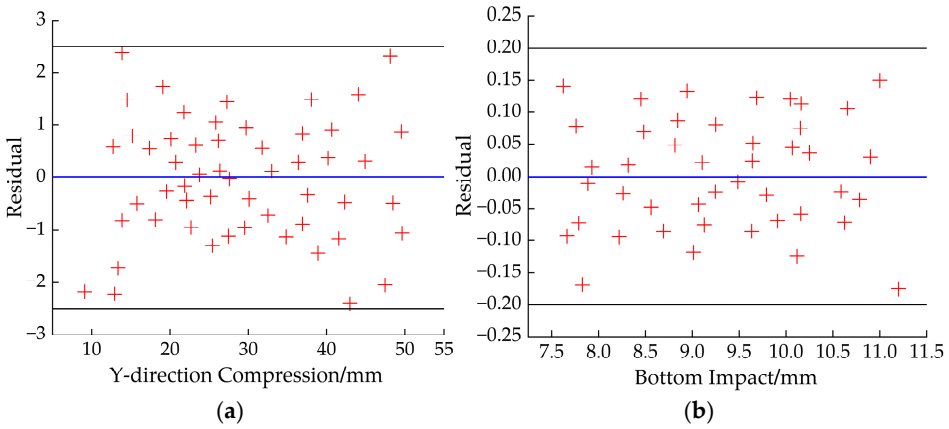


Figure 22. Residual plots of surrogate models: (**a**) Y direction compression residual plot; (**b**) Bottom impact residual plot.

As shown in the residual plots, the residuals of the surrogate models exhibit an overall random distribution, with few extreme residuals and none appearing in the primary regions of interest, without affecting the optimization accuracy in these critical regions, indicating that the models possess good overall predictive capability.

4.3. Mathematical Model of Collaborative Optimization Based on the Improved Dynamic Relaxation Factor

For the multi-condition and multi-objective optimization of the CTB battery box, the system-level objectives are to minimize the component mass ($\min F_1(M)$), maximize the first-order modal frequency ($\max F_2(f)$), and minimize the maximum random vibration stress ($\min F_3(\sigma)$). At the discipline level, the objective is to minimize the inconsistency function ($\min J_i$) between the subsystems and the system. Sub-discipline 1 constrains the maximum deformation of the side beam under X and Y direction pole compression with a 100 kN load; Sub-discipline 2 limits the maximum deformation of the bottom protection plate under bottom impact conditions; and Sub-discipline 3 constrains the maximum stress under three typical extreme operating conditions. The overall CO model and workflow are illustrated in Figure 23.

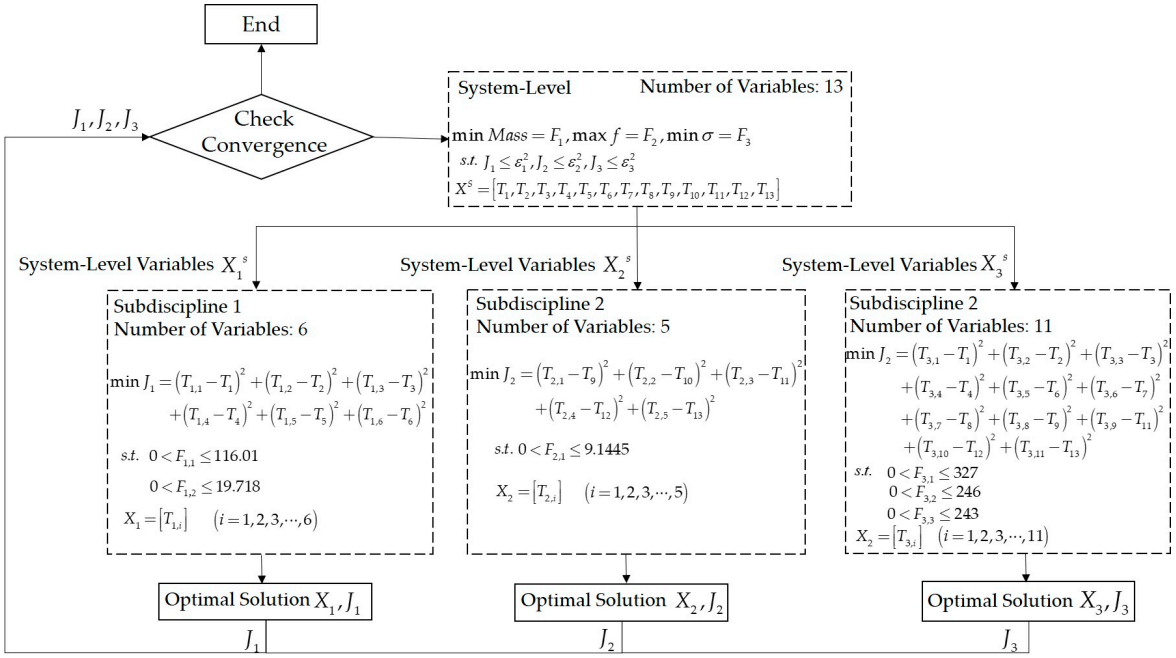


Figure 23. CO mathematical model and iterative process.

In the CO process, the consistency equality constraints between sub-discipline design variables(i.e., $j_i = 0,\ i = 1,2,3$) are difficult to strictly satisfy during iteration. To address this, an ε-relaxation factor is introduced to quantify the inconsistency between sub-discipline design variables $\boldsymbol{X_i}$ and system-level design variables $\boldsymbol{X^s}$, converting the original equality constraints into relaxed inequality constraints ($j_i \le \varepsilon,\ i = 1,2,3$). The feasible domain of the system-level optimization is defined as the intersection region of the sub-discipline design points $\boldsymbol{X_1}$, $\boldsymbol{X_2}$, $\boldsymbol{X_3}$, each represented as a hypersphere with radius ε centered at the corresponding design point, as illustrated in Figure 24. In the multi-dimensional design space, the feasible domain is thus the intersection of all ε-radius hyperspheres centered at the sub-discipline design points.

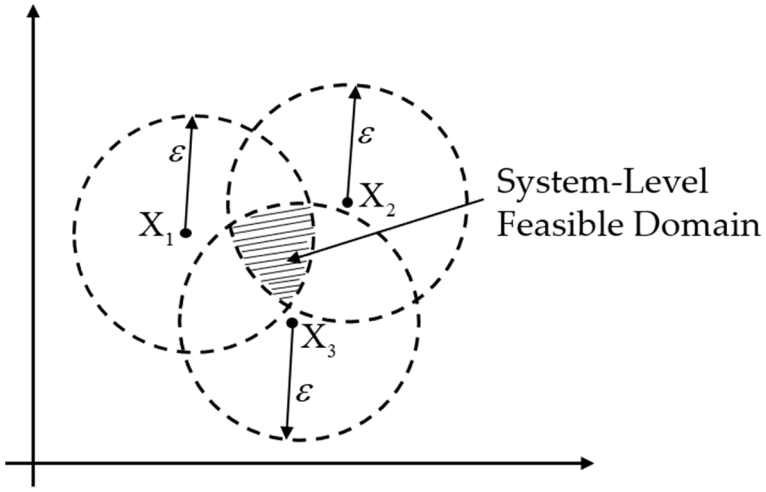


Figure 24. Schematic diagram of the Feasible domain based on the relaxation factor.

Although the relaxation factor method facilitates the solution of system-level optimization problems, determining an appropriate value is often challenging. The conventional dynamic relaxation-based CO algorithm primarily adjusts the relaxation factor based on inconsistent information among disciplines. In the early stages of iteration, this approach

may overly emphasize inter-disciplinary coordination, resulting in an excessively small relaxation factor when the disciplinary results are similar but significantly deviate from the system-level objectives, thereby affecting the system-level solution. To address this issue, the traditional relaxed CO algorithm is improved by incorporating difference information based on weight allocation, allowing the relaxation factor to account for both inter-disciplinary inconsistencies and those between the system and sub-disciplines.

After the k-th optimization iteration of the CO algorithm, each sub-discipline obtains its optimal design point $\boldsymbol{X_i}$. The inconsistency between any two sub-disciplines is defined using the norm concept as follows:

$$J_{ij}^{(k)} = \left\| \boldsymbol{X_i} - \boldsymbol{X_j} \right\| \tag{1}$$

where $J_{ij}^{(k)}$ represents the inconsistency between the optimization results of sub-disciplines i and j after the k-th iteration. For a CO problem with n sub-disciplines, there exists a total of $n(n-1)/2$ such norms $J_{ij}^{(k)}$.

$$J^{(k)} = \max\left\{ J_{ij}^{(k)} \right\},\ i, j = 1, 2 \cdots n,\ i \neq j \tag{2}$$

where $J^{(k)}$ represents the maximum deviation among the optimized design points of all sub-discipline.

After the k-th optimization iteration of the CO algorithm, the system-level optimal design point is $\boldsymbol{X^s}$, and the norm is defined as follows:

$$U^{(k)} = \left\| \boldsymbol{X^s} \text{-} \bar{\boldsymbol{X}} \right\| \tag{3}$$

$$\bar{\boldsymbol{X}} = \left(\frac{\sum_{i=1}^{n} \boldsymbol{X_{i1}}}{n}, \frac{\sum_{i=1}^{n} \boldsymbol{X_{i2}}}{n}, \ldots, \frac{\sum_{i=1}^{n} \boldsymbol{X_{ij}}}{n} \right) \tag{4}$$

where $U^{(k)}$ represents the inconsistency information between the system-level optimization result and the average value of the sub-discipline results after the k-th optimization iteration; n is the number of sub-disciplines associated with the design variables; and $\bar{\boldsymbol{X}}$ denotes the mean value of the optimal solutions of the n sub-disciplines after the k-th iteration.

The inconsistency information among sub-disciplines $J^{(k)}$ and that between the system and sub-disciplines $U^{(k)}$ are utilized to define the weighting coefficients λ_1 and λ_2. These coefficients are subsequently employed to adjust the discrepancies between the two types of inconsistency information, thereby constructing the relaxation factor ε, which is expressed as follows:

$$\lambda_1 = \frac{U^{(k)}}{U^{(k)} + J^{(k)}} \tag{5}$$

$$\lambda_2 = \frac{J^{(k)}}{U^{(k)} + J^{(k)}} \tag{6}$$

$$\varepsilon = \lambda_1 \times U^{(k)} + \lambda_2 \times J^{(k)} \tag{7}$$

where λ_1 and λ_2 serve as the correction coefficients for $U^{(k)}$ and $J^{(k)}$, respectively, and ε represents the modified relaxation factor. When the inconsistency between the system and sub-disciplines is pronounced, λ_1 guides the optimization process to focus on resolving this inconsistency, while appropriately reducing emphasis on handling the inconsistency among sub-disciplines. This expands the overlapping region among the sub-disciplines,

lowers the difficulty of the system-level solution, and drives the system-level optimum progressively toward the disciplinary optima. In contrast, λ_2 shifts the emphasis toward addressing the inconsistency among sub-disciplines, strengthening the handling of inter-disciplinary discrepancies. This encourages the optimal design points of each sub-discipline to converge toward a common location while simultaneously moving closer to the system-level optimum.

The inconsistent information is dynamically regulated by weighting factors λ_1 and λ_2 to adjust the relaxation factor ε, enabling the algorithm to automatically attenuate the influence of high-error disciplines and reinforce the effect of consistent information, thereby suppressing error accumulation during iteration and ensuring that the final optimized solution exhibits strong robustness against surrogate model errors.

5. Optimization Results and Validation

The NSGA-II algorithm can capture complex trade-offs arising from disciplinary coupling through hierarchical selection, effectively avoiding local optima within individual sub-disciplines. Therefore, NSGA-II is employed as the system-level optimizer. The Evolutionary Algorithm (EVO), with its population-based parallel search capability and strong computational stability, is adopted for all three sub-disciplines.

5.1. Multi-Condition Collaborative Optimization Results

In the system-level optimization using the NSGA-II algorithm, the population size was set to 1000, the number of generations to 150, and the crossover probability to 0.9. For the sub-discipline level solved by the Evolutionary Algorithm, the maximum number of evaluations was set to 200. Following the CO framework shown in Figure 14, a multi-condition CO of the battery box was performed using the CO method with an improved dynamic relaxation factor (IDRF) based on weighted difference information. After 124 iterations and 128,457 sample evaluations, the results converged. The Pareto front distribution of the system-level objectives, including mass M, first-order modal frequency f, and maximum random vibration stress σ, is shown in Figure 25.

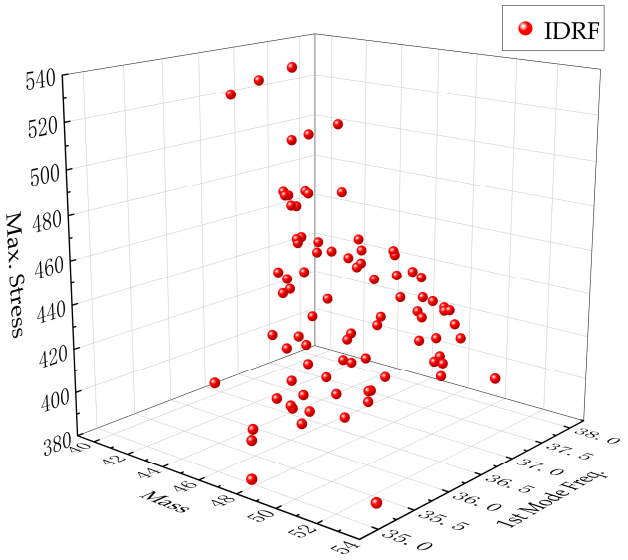


Figure 25. Pareto solution set of the CO framework with the IDRF.

Under identical system-level and sub-discipline optimization algorithms and parameter settings, the static relaxation factor (SRF) and conventional dynamic relaxation factor (DRF) strategies within the CO framework were compared, with the maximum number of

evaluations set to 150,000. The CO implementation with the SRF reached the maximum evaluation limit, while the one with the conventional DRF converged after 134,586 evaluations. The proposed CO framework incorporating the IDRF demonstrated higher computational efficiency. The obtained Pareto solution sets are shown in Figures 26 and 27.

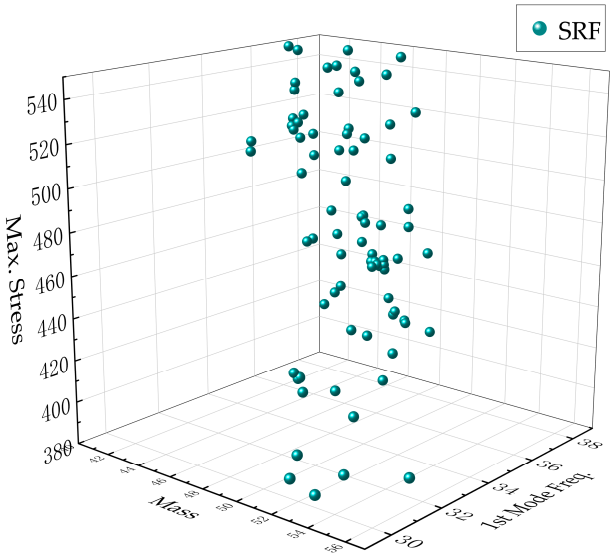


Figure 26. Pareto solution set of the CO framework with the SRF.

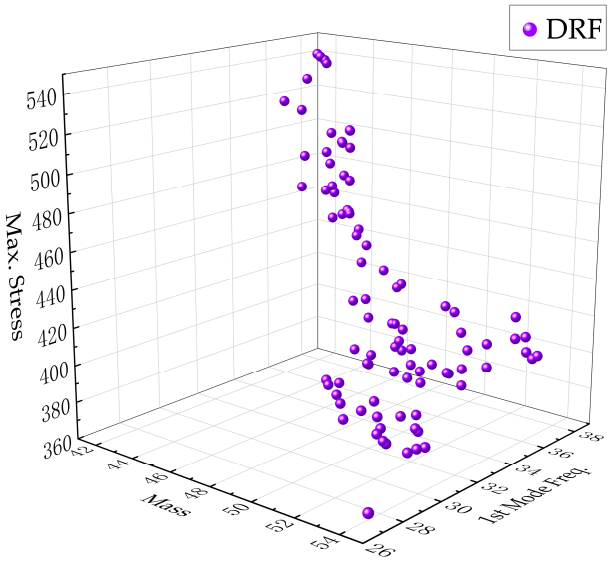


Figure 27. Pareto solution set of the CO framework with the DRF.

The performance of the algorithms was evaluated using three multi-objective assessment metrics: Generational Distance (GD), Inverted Generational Distance (IGD), and Spacing Metric (SP). Smaller GD and IGD values indicate better convergence and diversity, while a smaller SP value represents a more uniform distribution of the Pareto front [27]. The calculated GD, IGD, and SP indicators for the static relaxation CO method, conventional dynamic relaxation CO method, and improved dynamic relaxation CO method are shown in Figure 28.

The improved dynamic relaxation CO method outperforms both the static relaxation CO method and the traditional dynamic relaxation CO method. Specifically, the GD values were reduced by 67.49% and 35.92%, the IGD values by 68.75% and 16.67%, and the SP values by 23.49% and 32.35%, respectively. Therefore, this method exhibits superior

convergence and diversity, along with a more uniform Pareto front distribution, achieving the best overall performance.

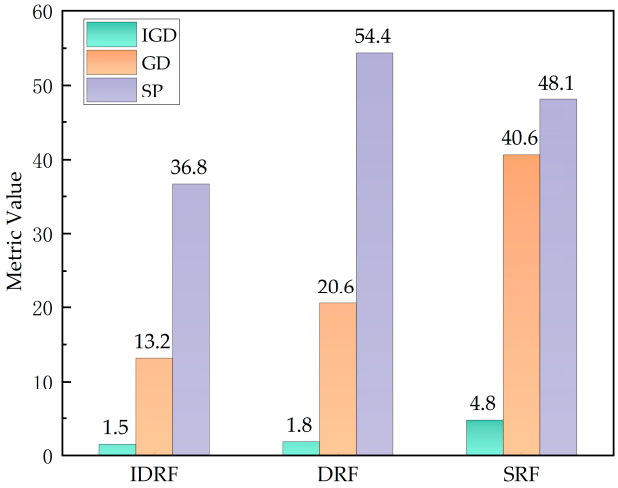


Figure 28. Evaluation metrics of different methods.

5.2. Multi-Attribute Decision-Making Based on the Entropy-Weighted TOPSIS Method

The obtained Pareto solutions are non-dominated, requiring a specific decision-making approach to identify the optimal solution. Existing decision-making methods mainly include Knee-Point Detection, Achievement Scalarizing Function (ASF), Compromise Programming (CP), and Entropy Weight-TOPSIS. Compared with the knee-point detection method, which relies solely on the geometric shape of the Pareto front, TOPSIS can incorporate objective weighting information, thereby balancing the decision-maker's actual preferences with the intrinsic characteristics of the data. Compared with the ASF and CP methods, which require predefined reference points or preference directions, TOPSIS considers both the positive and negative ideal solutions and ranks alternatives based on relative closeness, making the decision-making process more robust and reliable. The entropy-weighted TOPSIS method integrates the entropy weighting and TOPSIS approaches, effectively eliminating subjective weighting bias while dynamically reflecting variations in indicator importance. Therefore, the Entropy Weight-TOPSIS method was selected as a systematic decision-making tool to identify the final recommended solution from the Pareto solution set. Based on entropy calculations, the weighting ratios w_j of the optimization objectives were determined, and the corresponding system-level objective weights for the battery box are listed in Table 11.

Table 11. Entropy values and weight coefficients of optimization objectives.

Optimization Objective	F_1	F_2	F_3
Entropy Value	0.987	0.988	0.981
Weight Coefficient	0.314	0.263	0.422

The positive ideal solution S^+ and negative ideal solution S^- for each evaluation criterion were determined, and the Euclidean distance $sep_i^{\pm}$ between each evaluation scheme and the ideal solutions was calculated. Based on these distances, the closeness coefficient C_i for each scheme was obtained and ranked, as shown in Table 12. According to industrial standards, the design variables were rounded, and the optimized thickness parameters of the battery box components are presented in Table 13.

Table 12. Ranking results of optimized pareto solution set.

Serial Number	sep_i^+	sep_i^-	C_i	Ranking
1	0.142	0.454	0.762	1
2	0.277	0.367	0.570	77
...	...	...	...	...
87	0.386	0.424	0.523	81
88	0.221	0.393	0.641	53

Table 13. Thickness of battery box components before and after optimization.

No.	Before Optimization/mm	After Optimization/mm	Rounded/mm
T_1	1.2	1.580	1.6
T_2	1.2	0.836	0.8
T_3	1.2	1.425	1.4
T_4	1.2	0.825	0.8
T_5	1.0	0.837	0.8
T_6	1.0	0.933	0.9
T_7	0.8	0.602	0.6
T_8	0.7	0.503	0.5
T_9	1.0	0.714	0.7
T_{10}	0.8	0.507	0.5
T_{11}	0.8	0.591	0.6
T_{12}	1.5	2.262	2.3
T_{13}	2.3	1.663	1.7

5.3. Weight Sensitivity Analysis

To verify the robustness of the obtained optimal solution and avoid excessive dependence of the decision results on specific weight settings or data normalization methods, a sensitivity analysis of the decision results is required. Using the weighting coefficients in Table 11 as the baseline, uniform random perturbations within ±10% were applied to generate 100 sets of weight vectors, which were then normalized. Examples of the weight perturbations are shown in Table 14.

Table 14. Examples of Weight Coefficient Perturbations.

Group	w_1	w_2	w_3	Normalized Weights [w_1, w_2, w_3]
Baseline	0.314	0.263	0.422	[0.314, 0.263, 0.422]
1	0.329	0.270	0.398	[0.330, 0.271, 0.399]
2	0.306	0.256	0.431	[0.307, 0.257, 0.436]
3	0.311	0.288	0.400	[0.300, 0.277, 0.423]
...	...	...	...	...
99	0.322	0.260	0.426	[0.320, 0.258, 0.422]
100	0.299	0.269	0.409	[0.306, 0.275, 0.419]

TOPSIS was recalculated for the above 100 sets of perturbed weights, and the ranking performance of the original optimal solution was statistically analyzed. The statistical results of the weight sensitivity analysis are presented in Table 15. The results indicate that within a ±10% weight perturbation range, the original optimal solution maintained the first ranking in up to 97% of the trials, demonstrating extremely high ranking stability.

Table 15. Statistical Results of Weight Sensitivity Analysis.

Statistical Indicator	Value	Evaluation Criterion	Evaluation Result
Number of trials	100	—	—
Number of times ranked first	97	>90% indicates excellent	Excellent
Stability ratio	97%	/95% indicates high stability	Highly stable

5.4. Performance Verification of the Optimized Battery Box

Physical impact and vibration tests can directly verify the structural response and failure modes of a design under real operating conditions by comparing simulated and experimentally measured stress and deformation data, thereby enhancing engineering reliability. Due to time and cost constraints, physical testing was not conducted in this study; instead, an alternative validation strategy based on a validated simulation model was adopted. Based on the optimized design parameters, modal, random vibration, and extreme working-condition simulations were re-performed for the CTB high-strength steel roll-formed battery box. The comparison of the first six modal frequencies before and after optimization is presented in Table 16, showing overall improvements. The first-order modal frequency increased from 32.512 Hz to 37.178 Hz, representing a 14.4% improvement. Under random vibration conditions in the X, Y, and Z directions within the range of $-3\sigma_F \sim 3\sigma_F$, the maximum stresses were reduced by 5.56%, 36.45%, and 30.24%, respectively. Under the vertical bump, emergency braking on rough roads, and sharp turning on rough roads, the maximum stresses decreased by 31.05%, 30.97%, and 30.65%, respectively. The stress cloud diagrams for the random vibration and extreme operating conditions after optimization are shown in Figure 29.

Table 16. Comparison of the first six natural frequencies before and after optimization.

Order	Before Optimization/Hz	After Optimization/Hz
1	32.512	37.178
2	51.232	58.994
3	64.147	69.889
4	65.733	74.749
5	89.458	100.070
6	94.545	108.63

The optimized battery box was analyzed under compression and bottom impact conditions, with the results shown in Figures 30 and 31. Under X direction compression, the maximum deformation was 113.56 mm, representing a 2.11% reduction. Under Y direction compression, the maximum displacement of the box was 91.683 mm, with a side beam intrusion of 19.445 mm, both showing decreased deformation. During the bottom impact condition, the maximum displacement of the bottom guard plate was 9.102 mm, indicating improved protective performance. As the battery box is constructed from high-strength steel, the baseline design already possesses high stiffness, resulting in intrinsically low deformation responses and limited physical potential for further significant optimization. Therefore, the extent of improvement in deformation performance is naturally smaller than that of objectives that are more sensitive to design variables, such as modal frequencies.

Based on the Z-direction random vibration test PSD load spectrum specified in GB 38031-2025, the stress responses were obtained through frequency response analysis, and the fatigue life was predicted using the Dirlik method in conjunction with the Miner linear cumulative damage rule. The simulation results indicate that, under this loading environment, the predicted fatigue life at the critical structural location is 25.3 h, while the equivalent number of failure cycles derived from the same damage analysis is 1.4202

$\times 10^6$. The predicted life is approximately 2.1 times the specified test duration (12 h), demonstrating that the optimized battery box possesses sufficient fatigue safety margin. The fatigue life contour is shown in Figure 32.

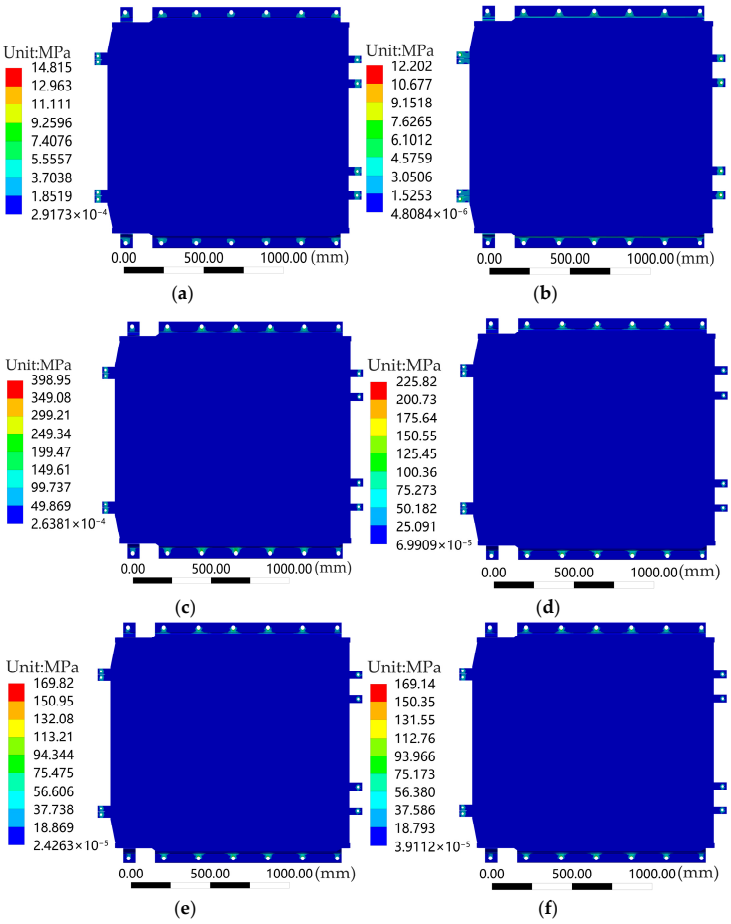


Figure 29. Stress cloud diagrams after optimization under random vibration and extreme conditions: (**a**) X direction random vibration; (**b**) Y direction random vibration; (**c**) Z direction random vibration; (**d**) Bumpy condition; (**e**) Bumpy emergency braking condition; (**f**) Bumpy sharp turn condition.

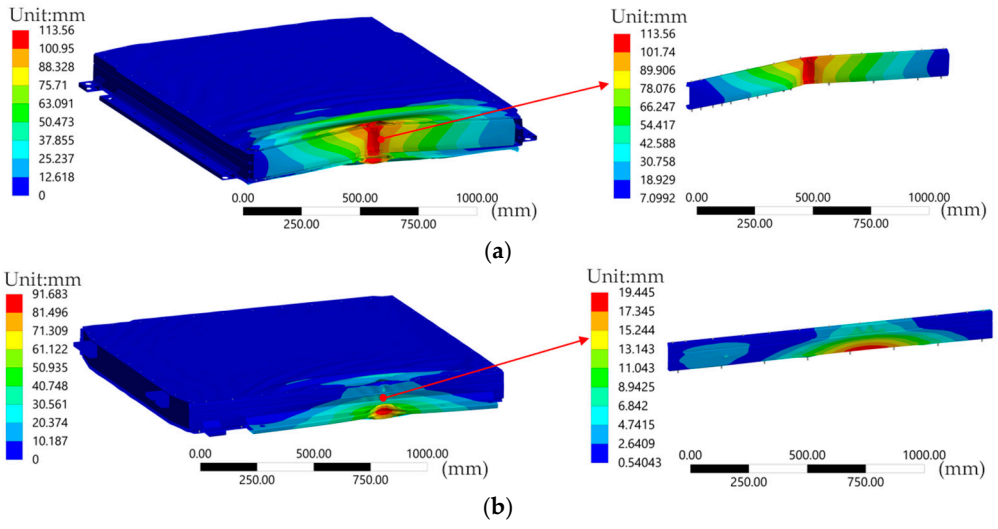


Figure 30. Displacement cloud diagrams of X and Y direction pole compression after optimization: (**a**) X direction; (**b**) Y direction.

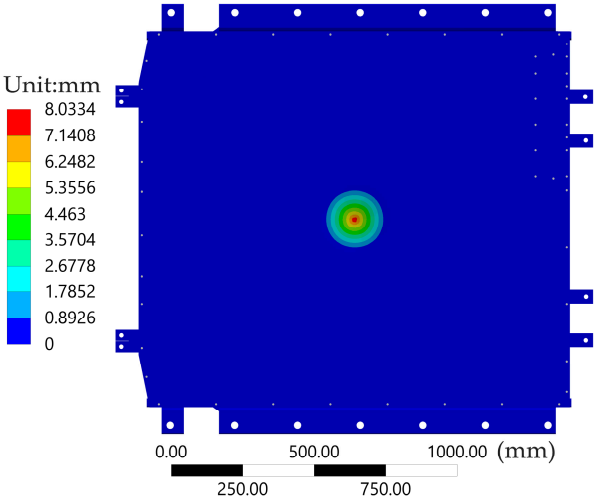


Figure 31. Displacement cloud diagram of bottom impact after optimization.

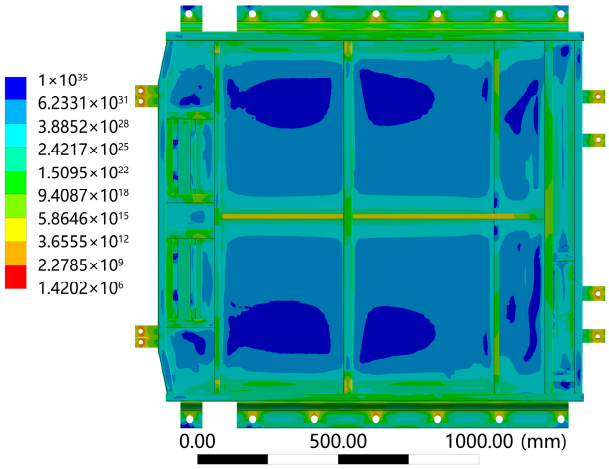


Figure 32. Fatigue life cloud diagram of battery box under Z-direction random vibration.

Before optimization, the vehicle curb mass was 1740 kg, the original battery pack mass was 443 kg, the battery box mass was 81.896 kg, and the CLTC-rated driving range was 530 km. After optimization, the mass of the CTB high-strength steel roll-formed battery box was reduced to 71.761 kg, corresponding to a mass reduction of 10.135 kg. The calculation formulas for the improvement ratio of the battery pack gravimetric energy density $\Delta\rho$ and the theoretical driving range gain ΔR are given as follows:

$$\Delta\rho = \frac{m_{p0} - m_{p1}}{m_{p1}} \times 100\% \tag{8}$$

$$\Delta R = R_0 \times \left(\frac{m_{v0} - m_{v1}}{m_{v1}} \times k \right) \tag{9}$$

where m_{p0} and m_{p1} are the battery pack masses before and after optimization, respectively; m_{v0} and m_{v1} are the vehicle curb masses before and after optimization, respectively; R_0 is the CLTC-rated driving range of the vehicle before optimization; and k is the mass-to-range conversion coefficient, taken as 0.7.

The calculation results indicate that this lightweight design can theoretically increase the battery pack gravimetric energy density by approximately 2.34% and extend the vehicle driving range by about 2.17 km.

6. Conclusions

To address the issues of low optimization efficiency and mutual interference among optimization objectives caused by coupled design variables in the multi-condition optimization of CTB battery boxes, a finite element simulation and multi-condition CO were conducted based on the requirements of GB 38031-2025. The entropy-weighted TOPSIS method was employed for solution selection, seamlessly integrating the optimization and decision-making processes to establish a comprehensive engineering design framework. The main conclusions are as follows:

(1) A finite element model of the CTB high-strength steel roll-formed battery box was established and validated through modal testing. Static, dynamic, and compression analyses confirmed that modal responses and extreme operating conditions satisfied design requirements. However, the maximum stress at the mounting beam exceeded the 550 MPa yield limit under random vibration, indicating the need for structural reinforcement in subsequent optimization.

(2) To enable parallel optimization across multiple operating conditions, a CO model was developed within a multi-condition design framework. System-level objectives included mass, first-order modal frequency, and maximum stress under random vibration. High-fidelity surrogate models were constructed via design of experiments, and an improved relaxation factor strategy based on weighted difference information was introduced, significantly reducing computational cost while improving optimization efficiency and robustness.

(3) The optimized CTB battery box achieved a 12.38% mass reduction and a 14.4% increase in first-order modal frequency. Maximum stresses under random vibration and extreme conditions, as well as peak deformations under X and Y direction column compression, were substantially reduced. These enhancements markedly improved both static and dynamic performance, providing a solid basis for comprehensive optimization of CTB high-strength steel roll-formed structures and supporting subsequent prototype manufacturing and experimental validation.

Although the surrogate models and optimization methods employed in this study demonstrated satisfactory performance, certain limitations remain. In terms of validation, due to constraints of the research timeline and experimental costs, this study primarily relied on simulation analyses and did not conduct physical vibration bench or crash tests; future work should supplement the findings with experimental verification. Methodologically, constructing surrogate models independently for different loading conditions may increase the complexity of multi-condition collaborative analysis, and the general applicability of the proposed improved CO method to broader engineering problems remains to be verified. These limitations do not compromise the reliability of the core conclusions derived from the simulations and provide directions for future research.

Author Contributions: Conceptualization, J.H. and S.L.; methodology, S.L. and K.M.; software, S.Z., J.L. and K.M.; vali-dation, J.H., S.L. and P.Q.; formal analysis, S.L., J.L. and K.M.; investigation, J.H., P.Q. and K.M.; resources, S.L., P.Q. and K.M.; data curation, S.L., J.L. and K.M.; writing—original draft preparation, J.H. and S.L.; writing—review and editing, J.H., S.L. and K.M.; visualization, S.Z. and J.L.; supervision, J.H. and P.Q.; project administration, J.H., S.Z. and J.L.; funding acquisition, J.H., S.Z. and P.Q.; All authors have read and agreed to the published version of the manuscript.

Funding: This research was funded by the Guangxi Key Technologies R&D Program, grant number GuiKeAB25069452.

Data Availability Statement: The original contributions presented in this study are included in the article. Further inquiries can be directed to the corresponding author.

Conflicts of Interest: Shichao Zhang, and Juncheng Lu are employees of Guangxi Huge Stone New Energy Technology Co., Ltd. The remaining authors declare that the research was conducted in the absence of any commercial or financial relationships that could be construed as a potential conflict of interest.

Abbreviations

The following abbreviations are used in this manuscript:

CTB	Cell-to-body
CO	Collaborative Optimization
PSD	Power spectral density
MDO	Multidisciplinary Design Optimization
SRF	Static relaxation factor
DRF	Dynamic relaxation factor
IDRF	Improved dynamic relaxation factor
RSM	Response surface methodology
OPM	Orthogonal polynomial method
RBF	Radial basis function
GD	Generational Distance
IGD	Inverted Generational Distance
SP	Spacing Metric

References

1. Lian, Y.B.; Yi, B.G.; Tian, H.S.; Yan, J.F.; Quan, Y. Research on Frontal Crashworthiness of Cell-to-Body Integrated Vehicle Structure. *Automot. Eng.* **2025**, *2*, 309–314.
2. Liu, W.F. Analysis of Production Process of New Energy Vehicle Battery Pack Lower Box. *Automob. Appl. Technol.* **2024**, *19*, 122–126.
3. *GB 38031-2025*; Electric Vehicles Traction Battery Safety Requirements. China Standards Press: Beijing, China, 2025.
4. Zhao, Y.; Sun, X.Y.; Chen, K.M.; Hao, J.B.; Hu, X.S.; Wang, Y.Q.; Wang, Y.W. Mechanical Performance Analysis of CTB Battery Pack Based on Reentrant Triangular Microstructure. *J. Southwest Univ. Nat. Sci. Ed.* **2025**, *47*, 2–12.
5. Qiao, H.J.; Dai, D.C.; Tu, J.F.; Zhang, J. Structural Safety Analysis and Optimization of a Power Battery Pack Box. *Chin. J. Power Sources* **2023**, *47*, 1064–1068.
6. Li, J.; Hu, G.; Chen, J. Analysis and Optimization of Fatigue Caused by Vibrations in the Quick-Replacement Battery Box for Electric Vehicles. *World Electr. Veh. J.* **2023**, *14*, 226. [CrossRef]
7. Duan, L.B.; Zhang, Y.; Du, Z.P.; Liu, Y.G.; Meng, X.X.; Tian, G.N.; Zheng, H.Y.; Wu, C. Research on Lightweight Design of CTB Battery Pack Cover Assembly Based on VRB/OW-GFRP Hybrid Structure. *Automot. Eng.* **2024**, *46*, 290–299.
8. Zeng, Q.H.; Zhang, X.S.; Ma, Y.J. Research and Analysis of Silicone Foam Sealing in CTB Structure. *Mater. Rep.* **2024**, *38*, 583–586.
9. Zhang, Y.; Chen, S.; Shahin, M.E.; Niu, X.; Gao, L.; Chin, C.M.M.; Bao, N.; Wang, C.-T.; Garg, A.; Goyal, A. Multi-Objective Optimization of Lithium-Ion Battery Pack Casing for Electric Vehicles: Key Role of Materials Design and Their Influence. *Int. J. Energy Res.* **2019**, *44*, 9414–9437. [CrossRef]
10. Xiong, Y.; Pan, Y.; Wu, L.; Liu, B. Effective Weight-Reduction and Crashworthiness Analysis of a Vehicle's Battery-Pack System via Orthogonal Experimental Design and Response Surface Methodology. *Eng. Fail. Anal.* **2021**, *128*, 105635. [CrossRef]
11. Naresh, G.; Praveenkumar, T.; Madheswaran, D.K.; Solomon, J.M.; Kureli, S.G.; Kolhe, Y.K.; Lalvani, I.J.R. Advancing Structural Efficacy and Resonance Performance of Battery Enclosures through Multi-Objective Optimization. *J. Low Freq. Noise Vib. Act. Control.* **2024**, *43*, 1895–1909. [CrossRef]
12. Ma, C.; Xu, C.; Souri, M.; Hosseinzadeh, E.; Jabbari, M. Multi-Objective Optimisation of the Battery Box in a Racing Car. *Technologies* **2024**, *12*, 93. [CrossRef]
13. Arslan, M.; Karamangil, M.İ. Comprehensive Optimization and Design of an Electric Vehicle Battery Box Side Profile for Lightweight and Crashworthiness Using a Novel Hybrid Structure. *Appl. Sci.* **2025**, *15*, 2037. [CrossRef]
14. Yay, İ.; Demirci, E.; Özcan, A.R. Multi-Objective Optimization of Aluminum Foam-Filled Battery Boxes for Electric Vehicle Safety. *Lat. Am. J. Solids Struct.* **2025**, *22*, e8408. [CrossRef]
15. Wang, N.Z.; Qin, K.J.; Tang, L.; Shangguan, L.J.; Zhou, F.P.; Shangguan, W.B. Optimization Design of Electric Vehicle Battery Box Based on Response Surface Model. *J. South China Univ. Technol. Nat. Sci. Ed.* **2024**, *52*, 43–51.

16. Su, H.; Gong, C.L.; Gu, L.X. A Universal MDO Framework Based on the Adaptive Discipline Surrogate Model. *Int. J. Aerosp. Eng.* **2018**, *2018*, 9139267. [CrossRef]
17. Cui, X.; Panda, B.; Chin, C.M.M.; Sakundarini, N.; Wang, C.T.; Pareek, K. An Application of Evolutionary Computation Algorithm in Multidisciplinary Design Optimization of Battery Packs for Electric Vehicles. *Energy Storage* **2020**, *2*, e158. [CrossRef]
18. Hao, Q.; Li, H.L.; Cui, H.W.; Tian, Y.N.; Liu, Z.W. Multidisciplinary Optimization Design of Electric Vehicle Door Considering Side Pole Impact. *J. Automot. Saf. Energy* **2020**, *11*, 314–321.
19. Lu, W.L.; Huang, W.; Xu, E.Y.; Chen, M.Z.; Lan, K.J. Multi-Objective Optimization Design of Hydrogen Storage System for Fuel Cell Commercial Vehicle Based on Response Surface Methodology. *Mod. Manuf. Eng.* **2023**, *5*, 58–64.
20. Wu, C.; Xu, X.M.; Peng, J.F.; Wang, W.W. Study on Vibration Characteristics of Mode-Free Power Battery Pack. *Noise Vib. Control.* **2024**, *3*, 202–208.
21. Lan, F.C.; Huang, P.X.; Chen, J.Q.; Liu, J. Study on the Method of Structural Dynamic Modeling and Analyzing of the EV's Battery Pack. *J. Mech. Eng.* **2018**, *54*, 157–164. [CrossRef]
22. Wan, C.D.; Sun, Y.; Lu, C.Y.; Wang, M. Mechanical Analysis and Optimization of Cast Aluminum Box Structure for Power Battery. *Mach. Des. Manuf.* **2024**, *8*, 212–216, 222.
23. Li, Y.K.; Yu, W.Q.; He, D.F.; Zhang, H.; Hu, Z.L. Structural Analysis and Lightweight Design of Battery Box for Pure Electric Vehicles. *China Plast. Ind.* **2020**, *48*, 91–95.
24. Wang, P.J.; Xie, H.; Wang, H.Y. Lightweight Design of Power Battery Pack Structure for Electric Vehicles. *Automob. Technol.* **2019**, *12*, 29–33.
25. Wen, Q.G.; Song, B.W.; Wang, P. Research on Several Issues of Collaborative Optimization Algorithm Based on iSIGHT Software. *J. Northwestern Polytech. Univ.* **2013**, *1*, 145–149.
26. Yang, L.L. Research on Multidisciplinary Collaborative Optimization and Its Uncertainty and Multiobjectivity. Ph.D. Thesis, Shanghai Jiao Tong University, Shanghai, China, 2020.
27. Wang, W.; Li, X.X.; Liu, W.J.; Bian, H.Y.; Xing, F.; Wang, J. Research on Cleaning Modeling and Multi-Objective Optimization of Laser Cleaning Quality of 7075 Aluminum Alloy. *J. Mech. Eng.* **2025**, *3*, 422–439.

Disclaimer/Publisher's Note: The statements, opinions and data contained in all publications are solely those of the individual author(s) and contributor(s) and not of MDPI and/or the editor(s). MDPI and/or the editor(s) disclaim responsibility for any injury to people or property resulting from any ideas, methods, instructions or products referred to in the content.